


Article

Stabilizing the (003) Facet of Micron-Sized $\text{LiNi}_{0.6}\text{Co}_{0.2}\text{Mn}_{0.2}\text{O}_2$ Cathode Material Using Tungsten Oxide as an Exemplar

Yang Li ^{1,2,†}, Liubin Ben ^{1,3,4,†}, Hailong Yu ^{1,3,4}, Wenwu Zhao ^{1,3,4}, Xinjiang Liu ^{5,*} and Xuejie Huang ^{1,2,3,4,*} 

¹ Songshan Lake Materials Laboratory, Dongguan 520838, China; liyang_lnu@163.com (Y.L.); benliubin@iphy.ac.cn (L.B.); yuhailong@iphy.ac.cn (H.Y.); wwz@iphy.ac.cn (W.Z.)

² Department of Physics, Liaoning University, Shenyang 110036, China

³ Beijing National Laboratory for Condensed Matter Physics, Institute of Physics, Chinese Academy of Sciences, Beijing 100190, China

⁴ Center of Materials Science and Optoelectronics Engineering, University of Chinese Academy of Sciences, Beijing 100049, China

⁵ National Key Laboratory of Science and Technology on Power Sources, Tianjin Institute of Power Sources, Tianjin 300384, China

* Correspondence: xjliu@nklps.org (X.L.); xjhuang@iphy.ac.cn (X.H.)

† These authors contributed equally to this work.

Abstract: The structural stability of layered $\text{LiNi}_{1-x-y}\text{Co}_x\text{Mn}_y\text{O}_2$ cathode materials is critical for guaranteeing their excellent electrochemical cycling performance, particularly at elevated temperatures. However, the notorious $\text{H}_2\text{--H}_3$ phase transition along with associated large changes in the *c*-axis or (003) facet is the fundamental origin of the anisotropic and abrupt change in the unit cell and the degradation of the cycling performance. In this study, we coat micron-sized $\text{LiNi}_{0.6}\text{Co}_{0.2}\text{Mn}_{0.2}\text{O}_2$ (NCM) with tungsten oxide via atomic layer deposition and investigate the atomic-to-microscopic structures in detail via advanced characterization techniques, such as Cs-corrected scanning transmission electron microscopy. The results reveal that coated tungsten oxide is predominately accumulated on the (003) facet of NCM, with the migration of a small amount of W^{6+} into this facet, resulting in a reduction of Ni^{3+} to Ni^{2+} and the formation of a rock-salt-like structure on the surface. The electrochemical cycling performance of tungsten-oxide-coated NCM is significantly improved, showing a capacity retention of 86.8% after 300 cycles at 55 °C, compared to only 69.4% for the bare NCM. Through further structural analysis, it is found that the initial tungsten-oxide-coating-induced (003) facet distortion effectively mitigates the expansion of the *c*-lattice during charge, as well as oxygen release from the lattice, resulting in a lowered strain in the cathode lattices and a crack in the cathode particles after prolonged cycling.

Keywords: layered cathode material; atomic layer deposition; tungsten oxide coating; scanning transmission electron microscopy; electrochemical cycling



Citation: Li, Y.; Ben, L.; Yu, H.; Zhao, W.; Liu, X.; Huang, X. Stabilizing the (003) Facet of Micron-Sized $\text{LiNi}_{0.6}\text{Co}_{0.2}\text{Mn}_{0.2}\text{O}_2$ Cathode Material Using Tungsten Oxide as an Exemplar. *Inorganics* **2022**, *10*, 111. <https://doi.org/10.3390/inorganics10080111>

Academic Editor: Christian Julien

Received: 22 April 2022

Accepted: 28 July 2022

Published: 3 August 2022

Publisher's Note: MDPI stays neutral with regard to jurisdictional claims in published maps and institutional affiliations.



Copyright: © 2022 by the authors. Licensee MDPI, Basel, Switzerland. This article is an open access article distributed under the terms and conditions of the Creative Commons Attribution (CC BY) license (<https://creativecommons.org/licenses/by/4.0/>).

1. Introduction

Since the first commercialization of lithium-ion batteries (LIBs) in 1991, LIBs have attracted great attention for the applications in consumer electronics and electric vehicles [1,2]. With the increasing demand for high-energy-density and high-power-density batteries, it is necessary to develop new cathode materials to replace commercially expensive LiCoO_2 . $\text{LiNi}_{1-x-y}\text{Co}_x\text{Mn}_y\text{O}_2$ cathode materials have the advantages of high energy density and relatively low cost; nickel oxide is considered one of the most promising cathode materials for LIBs [3,4]. However, the cycle performance of the $\text{LiNi}_{1-x-y}\text{Co}_x\text{Mn}_y\text{O}_2$ cathode materials shows a gradual decrease with increasing the nickel content [5,6]. The mechanisms behind the degradation of performance have been extensively investigated and are attributed to the surface irreversible formation of NiO rock-salt-like phases, intergranular cracks, micro-strains, transition metal dissolution, etc. [7–12]. Among nickel-rich

materials, $\text{LiNi}_{0.6}\text{Co}_{0.2}\text{Mn}_{0.2}\text{O}_2$ (NCM) has many advantages, such as preparation in air, high lithium-ion diffusion coefficient, and a relatively stable structure [13–15]; however, degradation of the cycling performance of NCM still occurs, particularly during cycling at elevated temperatures, which needs to be solved for successful commercialization.

To improve the cycling performance of cathode materials, one common method is to coat the surface with oxides such as Al_2O_3 [16], SiO_2 [17], Li_3PO_4 [18], $\text{Mn}_3(\text{PO}_4)_2$ [19], $\text{Li}_{1.3}\text{Al}_{0.3}\text{Ti}_{1.7}(\text{PO}_4)_3$ [20], LiAlO_2 [21], and $\text{Li}_2\text{Si}_2\text{O}_5$ [22]. These results showed that the structural stability of the cathode materials was high, resulting in an improved electrochemical cycling performance. In addition to coating, doping cathode materials with various oxides is also a very effective method. Schipper et al. [23] reported that Zr doping can suppress the phase change of NCM from the layered structure to the spinel structure. Liu et al. [24] showed that Mo doping for NCM can suppress the loss of lattice oxygen, enhance the cation order, broaden the Li^+ migration channel, and improve the electrochemical performance under high voltages. Rao [25] reported that dual doping with Mg and Mn can suppress detrimental phase changes and mitigate the accumulation of cracks in Ni-rich material. Huang et al. [26,27] confirmed that Na and Mg doping can promote Li^+ migration and improve the rate performance of NCM.

Of various coating and doping elements, tungsten has attracted much interest recently, owing to its effect on the electrochemical performance of many cathode materials. Geng et al. [28] showed that 1% tungsten added to LiNiO_2 can greatly improve the charge-discharge capacity retention while also delivering a high specific capacity. Ryu et al. [29] reported that tungsten doping can overcome the inherent structural instability of LiNiO_2 and considerably improve its cycling stability and thermal properties without compromising the capacity. It is expected that tungsten doping can provide similar benefits for NCM cathodes. Park et al. [30] investigated tungsten doping and found it to considerably improve the cycling stability and chemical stability of $\text{Li}[\text{Ni}_{0.90}\text{Co}_{0.05}\text{Mn}_{0.05}]\text{O}_2$. Chen et al. [31] concluded that the coupling of the mature atomic-layer deposition (ALD) technique with fluidizing techniques can help provide uniform coating or a complete surface treatment of particles for better protection. Becker et al. [32] demonstrated that, compared to uncoated electrodes, surface-modified electrodes show fewer degradation effects, such as particle cracking on the electrode surface, and an improvement in the thermal stability of $\text{Li}[\text{Ni}_{0.80}\text{Co}_{0.10}\text{Mn}_{0.10}]\text{O}_2$ in the presence of an electrolyte.

In this study, we coated the surface of micron-sized NCM with tungsten oxide via ALD, which is capable of forming uniform layers with precise thickness control [33]. The detailed atomic-to-microscopic characteristics of NCM before and after coating were probed by advanced analytical techniques, including aberration-corrected scanning transmission electron microscopy (Cs-STEM) with electron energy loss spectroscopy (EELS), and energy-dispersive X-ray spectrometry (EDS). The effect of tungsten oxide coating on various facets of the NCM cathode material and the associated improvement in cycling performance are discussed.

2. Materials and Methods

2.1. Materials Preparation

The $\text{Ni}_{0.6}\text{Mn}_{0.2}\text{Co}_{0.2}(\text{OH})_2$ precursor for the preparation of micron-sized NCM obtained via the co-precipitation method has been reported in the literature [34]. Micron-sized NCM was produced by mixing the as-obtained precursor with $\text{LiOH}\cdot\text{H}_2\text{O}$ (Li:M ratio = 1.08:1) and then calcined at 950 °C for 10 h in pure oxygen to obtain the final product. Tungsten oxide coating (WO_3 -coating) was performed with a Nano 900 ALD instrument (Ensure Scientific) and WCl_6 as the tungsten source. The WO_3 -coated NCM powders were heated at 500 °C for 6 h under an oxygen flow before electrochemical cycling.

2.2. Structure and Morphology Characterization

A scanning electron microscope (SEM, Zeiss Gemini SEM 300) combined with energy-dispersive spectroscopy (EDS) was used to analyze the chemical composition on the surface of the NCM particles.

X-ray diffraction (XRD) was applied to study the crystal structure of the bare and WO₃-coated NCM powders. The XRD patterns were collected between 10° and 100° (2θ) at a rate of 0.02° per minute. The diffractometer was a Bruker D8 ADVANCE diffractometer with a Cu K_α radiation source ($\lambda_1 = 1.54056 \text{ \AA}$, $\lambda_2 = 1.54439 \text{ \AA}$). Rietveld refinement for XRD patterns was performed via the TOPAS Academic software, with a fitting model similar to that reported by Dahn et al. [35] and Delmas et al. [36] Chebychev background and the modified Thompson–Cox–Hastings pseudo-Voigt peak type were used during the refinement. To understand the change in the lattice parameters of the cathode materials in the fully charged state (first cycle), cathode powders were scraped from electrodes disassembled from coin-type half-cells and mixed with internal Si standard for XRD analysis. The lattice parameters of the electrochemically cycled samples were fitted by the Pawley method.

The surface element information was investigated with X-ray photoelectron spectroscopy (XPS) conducted via a K_α X-ray photoelectron spectrometer (Thermo Fisher) with an Al K_α source (1486.6 eV). The binding energy was calibrated with the C1s peak (284.8 eV) of an external carbon in a vacuum chamber. Peak fitting and quantitative evaluation were conducted using the XPSPEAK software, and the background was corrected using the Shirley method.

A ThermoFisher ICAP 7200 inductively coupled plasma optical emission spectroscopy (ICP-OES) instrument was used for the determination of elements, particularly W in the NCM cathode materials. The experiment was performed five times to obtain an averaged value.

To precisely understand the atomic-scale structure of NCM before and after the ALD coating of tungsten, a Cs-corrected scanning transmission electron microscope (JEOL ARM200, 200 kV) was used to characterize the particles prepared with a focused ion beam. EDS and electron energy loss spectroscopy (EELS) were also employed to investigate element information and oxidation. The collection semi-angle of the HAADF detector was 12–24 and 75–250 mrad.

2.3. Electrode Preparation

The electrodes for electrochemical cycling were prepared similar to that reported in the literature [34].

2.4. Electrochemical Cycling Test

Electrochemical cycling was performed at room temperature and 55 °C in the voltage range of 2.75–4.3 V on a LAND automatic battery tester (Wuhan Land Electronics, Wuhan, China).

3. Results

The morphology and crystal structure of the NCM cathode material before and after ALD coating with tungsten oxide were initially studied. The SEM images indicate that both the bare (Figure 1a₁,a₂) and the tungsten-oxide-coated (WO₃-coated) (Figure 1b₁,b₂) NCM particles were irregular, with size ranging from 1 to 4 μm. There was no obvious morphology change after tungsten oxide coating. The XRD patterns of the bare and WO₃-coated NCM cathode materials are shown in Figure 1c. In general, all the cathode materials exhibited similar diffraction patterns, with the main peaks indexed to the standard layered LiNiO₂ structure (space group R-3m) [37]. Typical features, such as the splitting of the (006)/(012) and (108)/(110) peaks, were evident for both the cathode materials, indicating the highly ordered layered structure [38]. To obtain more detailed lattice parameters of the bare and WO₃-coated NCM cathode materials, Rietveld refinement was performed using XRD data. The refined unit-cell parameters were $a = 2.8666(3) \text{ \AA}$, $c = 14.2066(1) \text{ \AA}$, and $V = 101.107(2) \text{ \AA}^3$ for the bare NCM, which are in good agreement with those reported

previously [39,40]. After tungsten oxide coating, the refined unit-cell parameters were $a = 2.8701(1) \text{ \AA}$, $c = 14.2133(2) \text{ \AA}$, and $V = 101.396(2) \text{ \AA}^3$. The detailed refinement parameters are shown in Table S1. The slightly increased unit cell is attributed to the migration of a small amount of W^{6+} into the lattice of NCM during the post-ALD heat treatment at $500 \text{ }^\circ\text{C}$, as will be shown later. Note that no additional reflections related to WO_3 were observed for WO_3 -coated NCM, possibly due to the small coating amount.

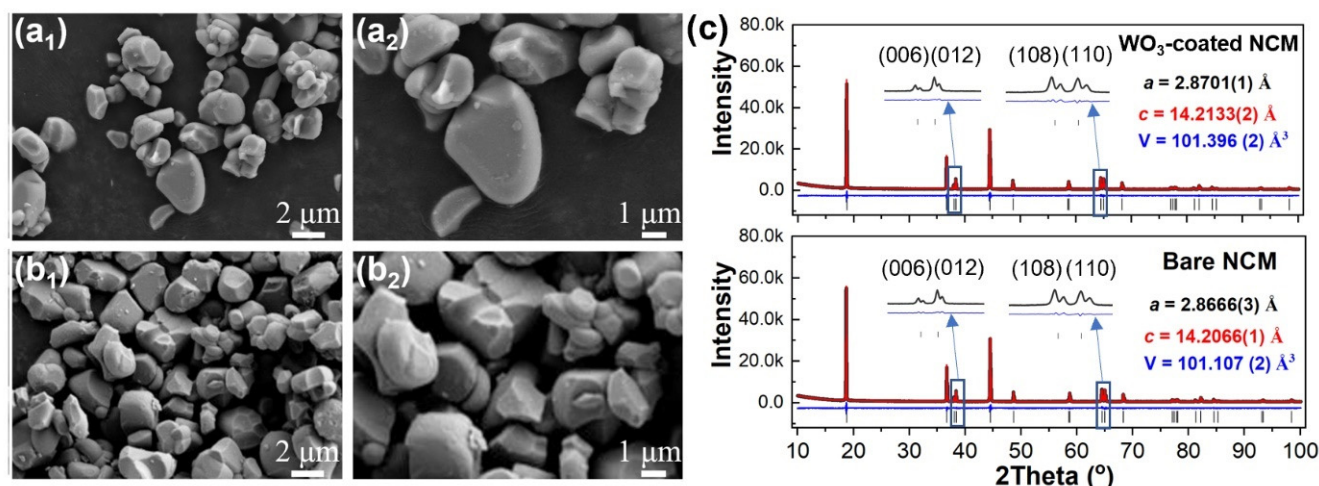


Figure 1. Morphology and XRD refinement of bare and WO_3 -coated NCM cathode materials. SEM images of (a₁,a₂) bare and (b₁,b₂) WO_3 -coated NCM cathode materials. (c) Rietveld refinement of XRD patterns for bare and WO_3 -coated NCM cathode materials. R_{wp} , R_p , gof and χ^2 for bare NCM are 4.63, 3.57%, 1.48, and 2.22 and for WO_3 -coated NCM are 4.84%, 3.70%, 1.54 and 2.40, respectively.

The element distribution of the bare and WO_3 -coated NCM cathode materials were investigated with SEM-EDS mapping, which showed a homogenous distribution of Ni, Co, Mn, and W elements (Figure 2a₁,a₂,b₁,b₂). To further understand the surface element information, particularly of tungsten, XPS was performed, and the results of the WO_3 -coated NCM materials are shown in Figure 2c₁,c₂. After tungsten oxide coating, two characteristic peaks at 35.43 and 37.66 eV associated with W^{6+} appeared, indicating the presence of WO_3 on the NCM particle surface after ALD coating [15]. The detailed tungsten composition in the WO_3 -coated NCM was $0.48 \pm 0.02 \text{ wt\%}$, as verified through ICP-OES.

The above results confirm the presence of a small amount of WO_3 on the surface of the NCM after ALD coating, without significantly altering the general morphology and layered structure of NCM. To understand the exact atomic-scale structure and element information before and after the ALD coating of tungsten oxide, the micron-size particles of bare and WO_3 -coated NCM were cut by a focused ion beam, and the regions of interest (ROIs) were precisely selected (Figure 3a) and investigated in detail by STEM. In general, two ROIs from each sample were investigated, i.e., a purple-boxed region (ROI-A) and a green-boxed region (ROI-B) for the bare NCM. The ROI-A exhibited a standard arrangement of transition metal (TM) atoms viewed along the [100] zone axis (Figure 3b₁) [41–44]. There was no evidence of any structural distortion via the migration of TM ions into the Li layer, as shown by the magnified region of Figure 3b₂. Similarly, STEM images of ROI-B also show a standard arrangement of TM atoms viewed along the [100] zone axis, without strong evidence of a contrast in the Li layer in the surface region (Figure 3c₁,c₂). The standard arrangements of the atoms in the ROI-A and B were also confirmed by line profiles (Figure 3d). In addition, based on the arrangement of TM atoms, the crystallographic [003] direction and (003) plane are indexed, as shown in Figure S4. This indicates that TM atoms are also arranged parallel to the (003) plane.

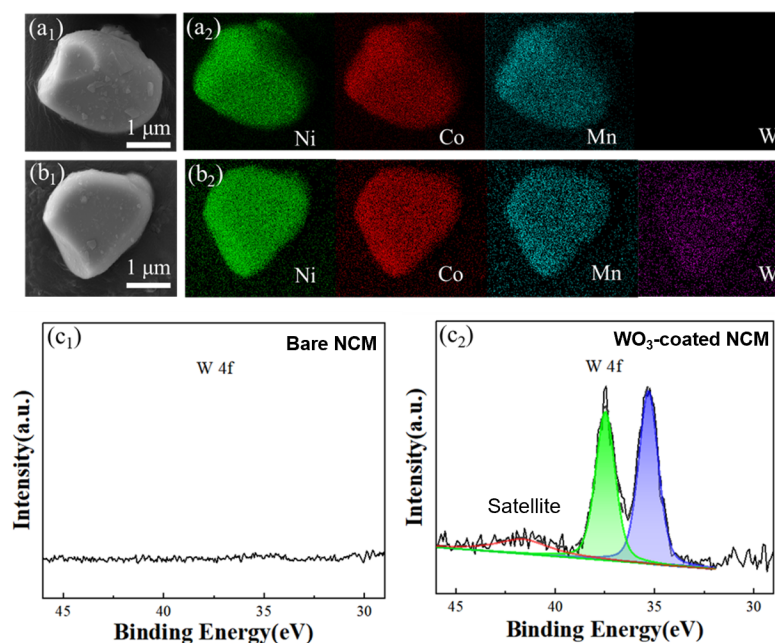


Figure 2. SEM images and element mapping of bare and WO_3 -coated NCM cathode materials (a_1, a_2, b_1, b_2). Surface XPS analysis of bare and WO_3 -coated NCM cathode powders. (c_1) W 4f of the bare NCM and (c_2) fitting of W 4f for the WO_3 -coated NCM cathode materials.

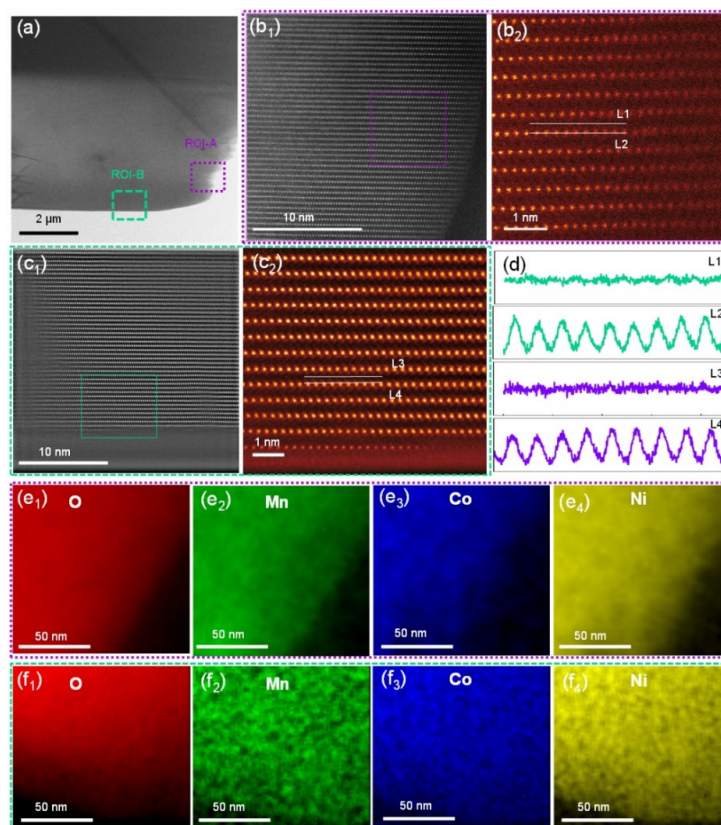


Figure 3. (a) A low-magnification STEM-HAADF image of the bare NCM particle. (b_1, b_2) Atomic-scale STEM-HAADF images of the surface of the bare NCM particle, as indicated by the purple box (ROI-A) in panel a; (c_1, c_2) atomic-scale STEM-HAADF images of the bare NCM particle, as indicated by the green box (ROI-B) in panel a. (d) Line profiles for the L1/L2 lines in panel b_2 and L3/L4 lines in panel c_2 . (e_1 – e_4) STEM-EDS mapping of elements O, Mn, Co, and Ni in the purple boxed region in panel a. (f_1 – f_4) STEM-EDS mapping of elements O, Mn, Co, and Ni in the green boxed region in panel a.

Elemental distribution in the ROI-A and ROI-B was performed with STEM-EDS. As shown in the O (Figure 3e₁), Mn (Figure 3e₂), Co (Figure 3e₃) and Ni (Figure 3e₄) maps for ROI-A and the O (Figure 3f₁), Mn (Figure 3f₂), Co (Figure 3f₃), and Ni (Figure 3f₄) maps for ROI-B, the compositions of these elements in both regions were distributed homogeneously. The oxidation state of the transition metal (TM) ions and the bonding nature between the TM ions could be detected by monitoring the fine structure changes of the core edges of these elements. The fitting of the as-obtained electron energy loss spectra (EELS) to the standard models obtained from the sample materials was performed to obtain the Ni concentration for each oxidation state. The details of the fitting procedure were reported previously [41,43]. The results show that the concentration of Ni²⁺ in ROI-A is 5.4% (Figure S1a), similar to that of 5.8% in ROI-B (Figure S1b). The limited presence of Ni²⁺ is also in agreement with the oxygen pre-peak in the K edge EELS spectra, showing a high intensity of the pre-peak (Figure S1c,d), suggesting limited oxygen deficiency in the bare NCM lattice.

Further STEM analysis was performed for WO₃-coated NCM cathode material to understand the effect of tungsten oxide coating on the atomic-scale structure. Two ROIs, i.e., purple-boxed region ROI-C and green-boxed region ROI-D, as shown in Figure 4a₁, were selected for detailed analysis. Unlike the bare NCM, as shown above, both the ROI-C and D regions exhibited increased atomic-scale structure distortion by the migration of TM atoms to the Li-layer to form the rock-salt-like structure (Figure 4b₁,b₂,c₁,c₂, respectively) [42,43,45]. Furthermore, the rock-salt-like structure was ~10 nm in ROI-D (Figure 4c₁), while it was only a few atomic layers in ROI-C (Figure 4b₂). The arrangement of atoms in ROI-C and D are shown by line profiles (Figure 4d), demonstrating that the clear rock-salt-like structure induced a sharp contrast in the Li-layer (L4) in ROI-D.

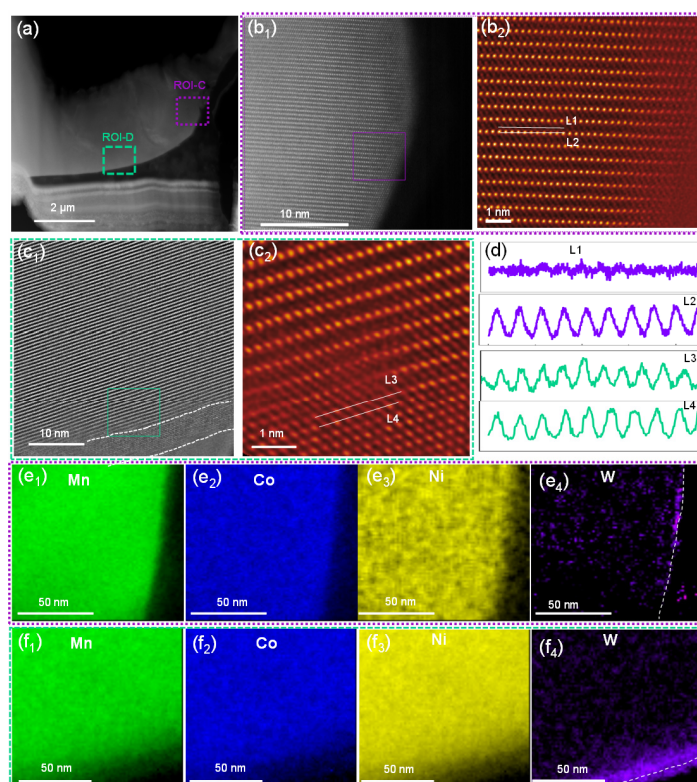


Figure 4. (a) A low-magnification STEM-HAADF image of the WO₃-coated NCM cathode particle. (b₁,b₂) Atomic-scale STEM-HAADF images of the surface of the WO₃-coated NCM cathode particle, as indicated by the purple box in panel a; (c₁,c₂) atomic-scale STEM-HAADF images of the WO₃-coated NCM particle, as indicated by the green box in panel a. (d) Line profiles for the L1/L2 lines in panel b2 and L3/L4 lines in panel c2. (e₁–e₄) STEM-EDS mapping of elements Mn, Co, Ni, and W in the purple boxed region in panel a. (f₁–f₄) STEM-EDS mapping of elements Mn, Co, Ni, and W in the green boxed region in panel a.

Elemental distribution mapping of ROI-C and ROI-D regions was also performed with STEM-EDS. As shown by the Mn (Figure 4e₁), Co (Figure 4e₂), Ni (Figure 4e₃), and W (Figure 4e₄) maps for ROI-C and the Mn (Figure 4f₁), Co (Figure 4f₂), Ni (Figure 4f₃), and W (Figure 4f₄) maps for ROI-D, the compositions of these Mn, Co, and Ni elements in both regions were distributed homogeneously; however, the W element predominated and was accumulated on the surface of ROI-D (Figure 4f). The fitting of the as-obtained EELS to the standard models showed that the concentration of Ni²⁺ in ROI-C was 8.4% (Figure S2a), while it was 25.8% in ROI-D (Figure S2b). The increased Ni²⁺ was also in agreement with the oxygen K-edge EELS spectra, showing a reduced intensity in the oxygen pre-peak, particularly in ROI-D (Figure S2c,d), suggesting an oxygen deficiency in the lattice in this region [46].

To further explore the effect of tungsten oxide coating on WO₃-coated NCM for practical use, electrochemical tests were conducted on the bare and WO₃-coated NCM half-cells. The results of the electrochemical results are shown in Figure 5. The half-cells were initially cycled at room temperature (RT) with a C-rate of 0.1 C for five cycles at a voltage range of 2.75–4.3 V. The initial discharge capacity of the bare NCM was 174.5 mAh/g at 0.1 C at RT (Figure 5a). After tungsten oxide coating, WO₃-coated NCM displayed an initial discharge capacity of 165.1 mAh/g at 0.1 C (RT). The prolonged RT cycling performance of the bare and WO₃-coated NCM half-cells are compared in Figure 5b. The bare NCM presented an initial 1 C discharge capacity of 165.5 mAh/g and a capacity retention of 93.7% after 100 cycles at RT. By contrast, WO₃-coated NCM displayed a slightly lower 1 C discharge capacity of 158 mAh/g but a higher capacity retention of 96.8% after 100 cycles at RT.

The corresponding dQ/dV curves in the first cycle at 0.1 C for the bare and WO₃-coated NCM are shown in Figure 5c, which exhibits similar redox peaks, indicating that the ALD coating of tungsten oxide does not have a significant effect on the electrochemical reaction during the charge–discharge process.

The rate capability of the bare and WO₃-coated NCM cathode materials between 0.1 and 5 C at RT are shown in Figure 5d. The bare NCM showed capacities of 174.5, 173.2, 169.4, 165.1, 155.2, and 127.6 mAh/g at 0.1, 0.2, 0.5, 1, 2, and 5 C, respectively. By contrast, WO₃-coated NCM exhibited lower capacities at lower C rates but higher capacities at higher C rates. For example, the capacities were 168.1 mAh/g, 166.3, 163.1, 158.2, and 153.2 mAh/g at 0.1–2 C but 134.2 mAh/g at 5 C. When the current density changed back to 0.1 C, WO₃-coated NCM half cells exhibited a strong structural tolerance for rapid lithium-ion exchange, showing a nearly complete recovery of discharge capacity. The improvement of the rate performance of NCM through tungsten oxide coating is mainly attributed to an improved structural stability, as will be shown later. By contrast, the reversible capacity for the bare NCM counterpart exhibited a recovery to 159.4 mAh/g when the current density changed back to 0.1 C, owing to the poor structural stability and associated decrease in the lithium-ion diffusion.

The bare and WO₃-coated NCM were further cycled at 55 °C to accelerate the degradation of cycling performance for better characterization, and the results are shown in Figure 5e,f. It is known that the reactions between cathode materials and trace amounts of HF in the electrolyte are enhanced at elevated temperatures [43,47,48], causing significant degradation of the cycling performance if the cathode structure is not stable. Both the bare and the WO₃-coated NCM showed a slightly increased discharge capacity during the first cycle at 55 °C because of the increased lithium-ion kinetics at elevated temperatures (Figure 5f). For the WO₃-coated NCM, the discharge capacity demonstrates an excellent retention of 86.9% after 300 cycles at 1 C (55 °C), compared to 69.4% for the bare NCM.

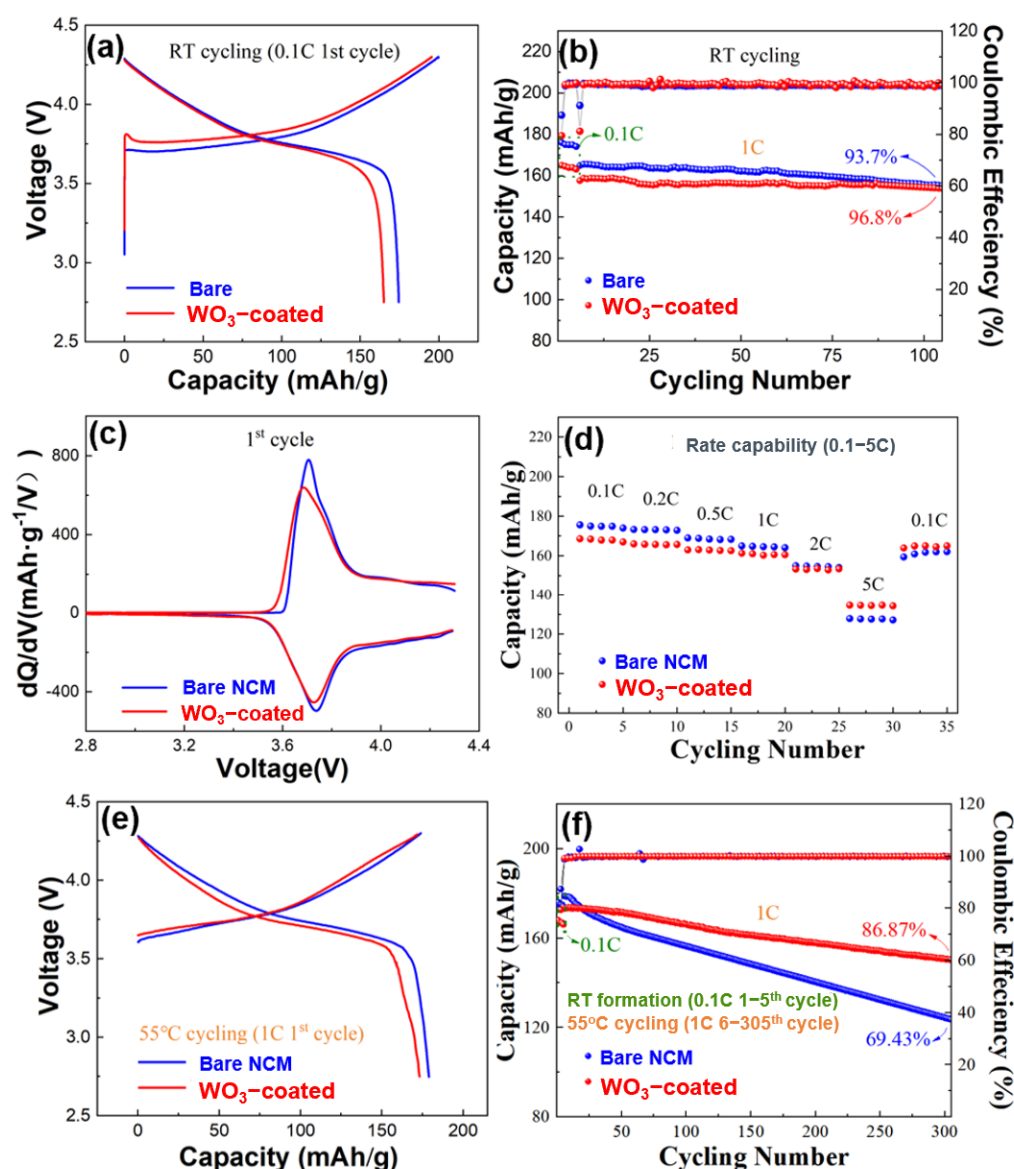


Figure 5. Electrochemical properties of the bare and WO₃-coated NCM half-cells. (a) Charge-discharge curves in the first cycle at 0.1 C (RT), (b) discharge capacity retention for the 6th–105th cycles at RT (1–5th at 0.1 C), (c) dQ/dV curves for the first cycle at RT, (d) discharge capacity at 0.1–5 C for 5 cycles at each C-rate, (e) charge–discharge curves in the first cycle at 55 °C and (f) discharge capacity retention at 55 °C for the 6th–305th cycles (0.1 C for the 1st–5th cycles at RT).

To understand the structural degradation of the NCM after prolonged cycling, typical electrodes were disassembled after 300 cycles at 55 °C in an argon-filled glove box for morphology analysis with SEM. As shown in Figure 6a₁,a₂, after 300 cycles at 55 °C (1 C), clear cracks were evident for the bare NCM cathode particles, ranging from the center to the edge of the particles. STEM-HAADF images of the 55 °C cycled bare NCM (Figure 6c₁,c₂) also reveal that the atomic-scale crack originating in the bulk region was parallel to the (003) plane. The oxygen K-edge EELS spectra showed that the intensity of the pre-peak was diminished, indicating significant oxygen loss from the lattice in the bulk region near the crack (Figure S3a). Compared with bare NCM, there was no evidence of cracks observed through SEM in the WO₃-coated NCM cathode particles (Figure 6b₁,b₂). STEM-HAADF images of the 55 °C cycled WO₃-coated NCM (Figure 6d₁,d₂) also revealed excellent atomic-scale arrangement of atoms in the bulk region. The oxygen K-edge EELS spectra showed that the intensity of the pre-peak was high, indicating no significant oxygen loss from the

lattice in the bulk region (Figure S3b). These observations confirm that the ALD coating of tungsten oxide significantly improved the stability of the NCM cathode material, alleviating particle breakage during cycling and consequently improving the cycling stability.

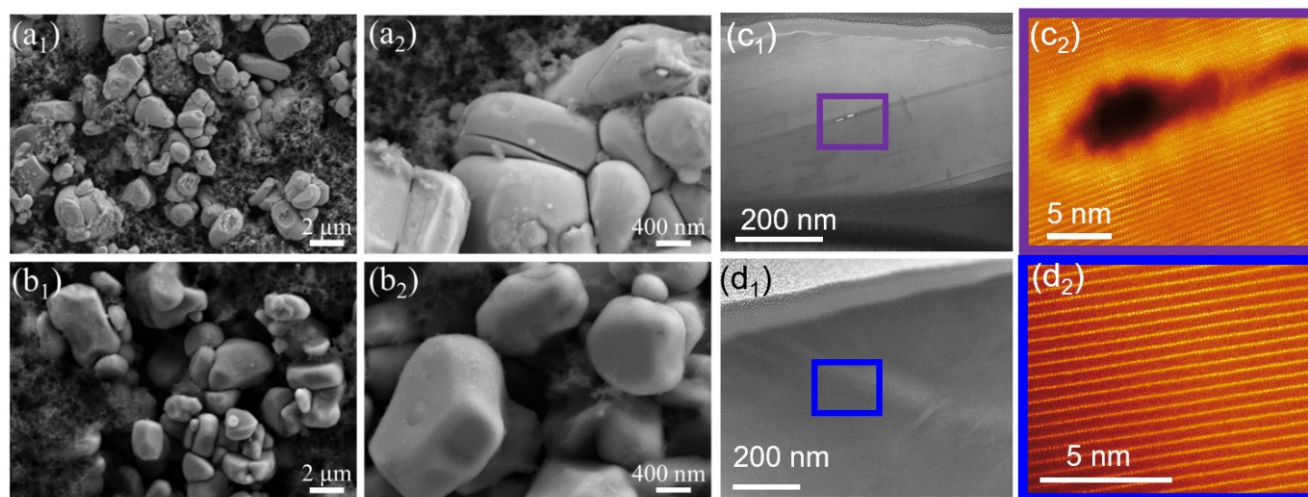


Figure 6. SEM images of (a₁,a₂) bare and (b₁,b₂) WO₃-coated NCM cathode materials after 300 cycles at 55 °C (1 C). (c₁,c₂) Low- and high-magnification STEM-HAADF images of bare NCM after 300 cycles showing a clear atomic-scale crack parallel to the (003) plane. (d₁,d₂) Low- and high-magnification STEM-HAADF images of WO₃-coated NCM after 300 cycles showing no evidence of cracks at the atomic scale.

4. Discussion

Based on the above detailed atomic-to-microscopic structure analysis and electrochemical cycling of the bare and WO₃-coated NCM, the improved cycling performance of NCM after ALD coating of tungsten oxide is mainly attributed to its effective inhibition of cycling-induced cracks [49,50]. The formed cracks expose fresh surfaces to the electrolyte, causing the formation of cycling-induced rock salt and the dissolution of TM ions in the electrolyte, and consequently, the rapid degradation of the cycling performance [51–53]. These adverse effects are further enhanced at elevated temperatures, owing to the increased amount of HF in the electrolyte, thus causing the rapid degradation of the cathode structure, and consequently, the cycling performance [47,48]. Furthermore, the loss of oxygen from the lattice, as clearly observed in the crack region (Figure S3a), results in the oxidation of the electrolyte and further formation of HF [46,54]. This, in turn, accelerates the structural distortion and degradation of the cycling performance. Thus, the bare NCM exhibits a much poorer capacity retention than WO₃-coated NCM, as observed in Figure 5f.

The formation of cracks in layered cathode materials may be attributed to many factors, with the main factor being anisotropic and abrupt lattice changes, which in turn induce strains and the formation of cracks. The anisotropic lattice changes during cycling are usually much greater along the *c*-axis than the *a*-axis. In an extreme case, pure LiNiO₂ showed $\Delta a = 2.0\%$ and $\Delta c = 7.9\%$ in the fully charged state. The repeated expansion/shrinkage of the (003) facet during lithium extraction (charging)/insertion (discharging) is the fundamental origin for cracks formed perpendicular to the *c*-direction or parallel to the (003) facet [3,49,50]. Though the lattice changes were less significant in NCM here, which contained 20 at % Co and 20 at % Mn, the change in Δc was still 1.81% in the fully charged state (14.2066 to 14.4641 Å), Figure S5a, which led to cracks parallel to the (003) facet after repeated cycles, as may be clearly observed through the STEM-HAADF images in Figure 6. In shape contrast, after the ALD coating of tungsten oxide, a small amount of W⁶⁺ migrated to the lattice, forming a ~10 nm-surface distorted rock-salt structure parallel to the (003) facet (Figure 4). Note that the exact origin for the (003) facet preferred for W⁶⁺ migration is not clear but is likely attributed to the minimization

of surface energy, as suggested by previous theoretical modeling works [55]. Though this surface structural distortion led to a sacrifice of the initial capacity at RT (~ 9 mAh/g lower at 0.1 C, RT, Figure 5a), the changes in the c -axis were significantly reduced, with a Δc of only 0.7% in the fully charged state (14.2133 to 14.3070 Å), as shown in Figure S5b, and resulting in a reduced formation of cracks, as observed above. Meanwhile, the surface distorted rock-salt structure also impeded the release of oxygen during cycling (see Figure S3b) and improved the structural stability [56]. The effect of tungsten oxide coating on the NCM cathode material during cycling is summarized in Figure 7.

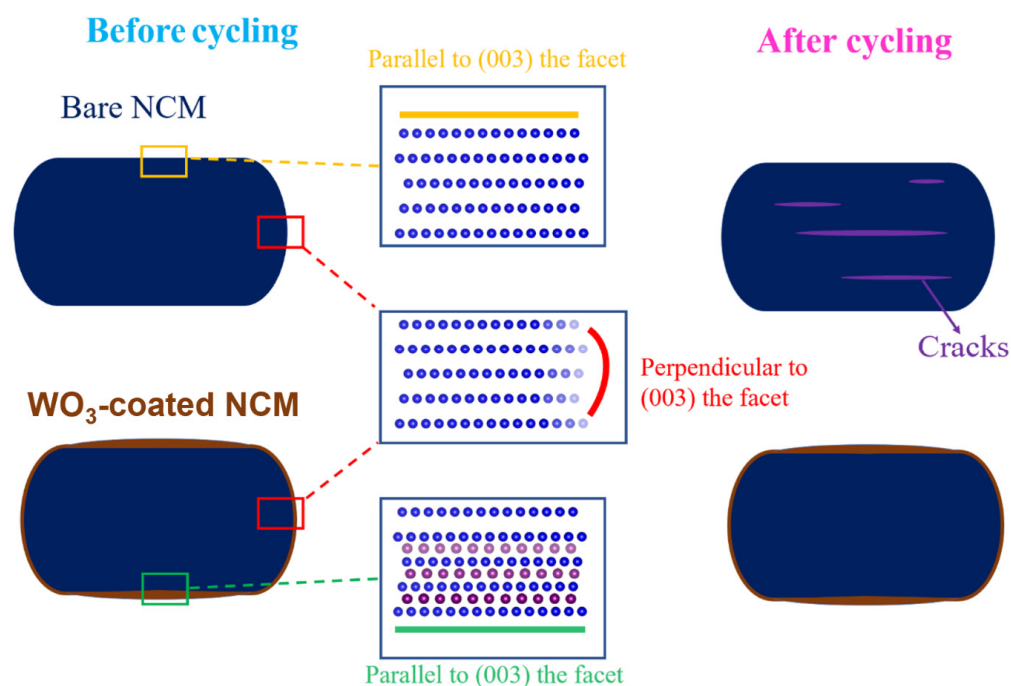


Figure 7. Schematic showing coated tungsten oxide stabilizing the (003) facet of the bare NCM and effectively mitigating lattice expansion along the lattice direction, resulting in fewer cracks after prolonged cycling.

5. Conclusions

In this work, a micron-sized $\text{LiNi}_{0.6}\text{Co}_{0.2}\text{Mn}_{0.2}\text{O}_2$ cathode material was prepared and coated with 0.48 ± 0.02 wt% WO_3 via atomic layer deposition using WCl_6 as the metal source. By employing advanced structural characterization techniques, WO_3 was mainly accumulated on the (003) facet, with a small amount of W^{6+} entering the ~ 10 nm surface, causing structural distortion and the formation of a rock-salt-like structure. This tungsten oxide coating induced initial structural distortion; however, it effectively mitigated a c -axis change during cycling and oxygen release from the lattice. Consequently, the electrochemical cycling performance of tungsten-oxide-coated NCM was significantly improved, showing a capacity retention of 86.8% after 300 cycles at 55 °C, compared to only 69.4% for the bare NCM.

Supplementary Materials: The following supporting information can be downloaded at: <https://www.mdpi.com/article/10.3390/inorganics10080111/s1>, Table S1. Rietveld refinement parameters for the bare and WO_3 -coated NCM cathode materials before cycling. Figure S1. EELS Ni L edge and O K edge spectra for uncycled bare NCM from (a,c) ROI-A and (b,d) ROI-B. Figure S2. EELS Ni L edge and O K edge spectra for uncycled WO_3 -coated NCM from (a,c) ROI-C and (b,d) ROI-D. Figure S3. EELS oxygen K edge spectra from bulk region of cycled (a) bare and (b) WO_3 -coated NCM. Figure S4. (a) Crystal structure and (b) arrangement of TM ions of NCM layered cathode material viewed along the [010] zone axis. (c) A STEM-HAADF image showing arrangement of TM atoms with respect to the FIB-cut micron-sized particle. Based on the arrangement of TM atoms, the crystallographic

[003] direction and (003) plane are indexed. Figure S5. Pawley fitting of XRD patterns for 1st cycle fully charged (a) bare and (b) WO₃-coated NCM cathode powders scraped from electrodes.

Author Contributions: Conceptualization, X.H. and X.L.; methodology, L.B.; software, L.B.; validation, Y.L.; formal analysis, Y.L.; investigation, Y.L.; resources, H.Y. and W.Z.; data curation, Y.L.; writing—original draft preparation, L.B.; writing—review and editing, L.B.; visualization, Y.L.; supervision, X.H.; project administration, X.H.; funding acquisition, X.H., Y.L. and L.B. contributed equally to this work. All authors have read and agreed to the published version of the manuscript.

Funding: This work was supported by the National Key Research and Development Program of China (grant no. 2019YFA0705101) and the National Natural Science Foundation of China (grant No. 22179144).

Institutional Review Board Statement: Not applicable.

Informed Consent Statement: Not applicable.

Data Availability Statement: Not applicable.

Acknowledgments: The authors would like to thank Ministry of Science and Technology and National Natural Science Foundation of China for funding.

Conflicts of Interest: The authors declare no conflict of interest.

References

1. Armand, M.; Tarascon, J.M. Building better batteries. *Nature* **2008**, *451*, 652–657. [[CrossRef](#)]
2. Tarascon, J.M.; Armand, M. Issues and challenges facing rechargeable lithium batteries. *Nature* **2001**, *414*, 359–367. [[CrossRef](#)] [[PubMed](#)]
3. Ryu, H.H.; Park, K.J.; Yoon, C.S.; Sun, Y.K. Capacity Fading of Ni-Rich LiNi_xCo_yMn_{1-x-y}O₂ (0.6 ≤ x ≤ 0.95) Cathodes for High-Energy-Density Lithium-Ion Batteries: Bulk or Surface Degradation? *Chem. Mater.* **2018**, *30*, 1155–1163. [[CrossRef](#)]
4. Julien, C.M.; Mauger, A. NCA, NCM811, and the Route to Ni-Richer Lithium-Ion Batteries. *Energies* **2020**, *13*, 6363. [[CrossRef](#)]
5. Noh, H.J.; Youn, S.; Yoon, C.S.; Sun, Y.K. Comparison of the structural and electrochemical properties of layered LiNi_xCo_yMn_zO₂ (x=1/3, 0.5, 0.6, 0.7, 0.8 and 0.85) cathode material for lithium-ion batteries. *J. Power Sources* **2013**, *233*, 121–130. [[CrossRef](#)]
6. Ma, L.; Nie, M.Y.; Xia, J.; Dahn, J.R. A systematic study on the reactivity of different grades of charged LiNi_xMn_yCo_zO₂ with electrolyte at elevated temperatures using accelerating rate calorimetry. *J. Power Sources* **2016**, *327*, 145–150.
7. Liu, W.; Oh, P.; Liu, X.; Lee, M.J.; Cho, W.; Chae, S.; Kim, Y.; Cho, J. Nickel-Rich Layered Lithium Transition-Metal Oxide for High-Energy Lithium-Ion Batteries. *Angew. Chem.-Int. Ed.* **2015**, *54*, 4440–4457. [[CrossRef](#)] [[PubMed](#)]
8. Kim, N.Y.; Yim, T.; Song, J.H.; Yu, J.S.; Lee, Z. Microstructural study on degradation mechanism of layered LiNi_{0.6}Co_{0.2}Mn_{0.2}O₂ cathode materials by analytical transmission electron microscopy. *J. Power Sources* **2016**, *307*, 641–648. [[CrossRef](#)]
9. Manthiram, A.; Knight, J.C.; Myung, S.T.; Oh, S.M.; Sun, Y.K. Nickel-Rich and Lithium-Rich Layered Oxide Cathodes: Progress and Perspectives. *Adv. Energy Mater.* **2016**, *6*, 1501010. [[CrossRef](#)]
10. Min, K.; Kim, K.; Jung, C.; Seo, S.-W.; Song, Y.Y.; Lee, H.S.; Shin, J.; Cho, E. A comparative study of structural changes in lithium nickel cobalt manganese oxide as a function of Ni content during delithiation process. *J. Power Sources* **2016**, *315*, 111–119. [[CrossRef](#)]
11. de Biasi, L.; Kondrakov, A.O.; Gesswein, H.; Brezesinski, T.; Hartmann, P.; Janek, J. Between Scylla and Charybdis: Balancing Among Structural Stability and Energy Density of Layered NCM Cathode Materials for Advanced Lithium-Ion Batteries. *J. Phys. Chem. C* **2017**, *121*, 26163–26171. [[CrossRef](#)]
12. Li, W.D.; Liu, X.M.; Xie, Q.; You, Y.; Chi, M.F.; Manthiram, A. Long-Term Cyclability of NCM-811 at High Voltages in Lithium-Ion Batteries: An In-Depth Diagnostic Study. *Chem. Mater.* **2020**, *32*, 7796–7804. [[CrossRef](#)]
13. Saavedra-Arias, J.J.; Rao, C.V.; Shojan, J.; Manivannan, A.; Torres, L.; Ishikawa, Y.; Katiyar, R.S. A combined first-principles computational/experimental study on LiNi_{0.66}Co_{0.17}Mn_{0.17}O₂ as a potential layered cathode material. *J. Power Sources* **2012**, *211*, 12–18. [[CrossRef](#)]
14. Wei, Y.; Zheng, J.X.; Cui, S.H.; Song, X.H.; Su, Y.T.; Deng, W.J.; Wu, Z.Z.; Wang, X.W.; Wang, W.D.; Rao, M.M.; et al. Kinetics Tuning of Li-Ion Diffusion in Layered Li(Ni_xMn_yCo_z)O₂. *J. Am. Chem. Soc.* **2015**, *137*, 8364–8367. [[CrossRef](#)]
15. Chu, B.; You, L.; Li, G.; Huang, T.; Yu, A. Revealing the Role of W-Doping in Enhancing the Electrochemical Performance of the LiNi_{0.6}Co_{0.2}Mn_{0.2}O₂ Cathode at 4.5 V. *ACS Appl. Mater. Interfaces* **2021**, *13*, 7308–7316. [[CrossRef](#)] [[PubMed](#)]
16. Yoo, K.S.; Kang, Y.H.; Im, K.R.; Kim, C.S. Surface Modification of Li(Ni_{0.6}Co_{0.2}Mn_{0.2})O₂ Cathode Materials by Nano-Al₂O₃ to Improve Electrochemical Performance in Lithium-Ion Batteries. *Materials* **2017**, *10*, 1273. [[CrossRef](#)] [[PubMed](#)]
17. Cho, W.; Kim, S.-M.; Song, J.H.; Yim, T.; Woo, S.-G.; Lee, K.-W.; Kim, J.-S.; Kim, Y.-J. Improved electrochemical and thermal properties of nickel rich LiNi_{0.6}Co_{0.2}Mn_{0.2}O₂ cathode materials by SiO₂ coating. *J. Power Sources* **2015**, *282*, 45–50. [[CrossRef](#)]

18. Jo, C.-H.; Cho, D.-H.; Noh, H.-J.; Yashiro, H.; Sun, Y.-K.; Myung, S.T. An effective method to reduce residual lithium compounds on Ni-rich $\text{Li}[\text{Ni}_{0.6}\text{Co}_{0.2}\text{Mn}_{0.2}]\text{O}_2$ active material using a phosphoric acid derived Li_3PO_4 nanolayer. *Nano Res.* **2015**, *8*, 1464–1479. [[CrossRef](#)]
19. Chen, Z.; Kim, G.-T.; Guang, Y.; Bresser, D.; Diemant, T.; Huang, Y.; Copley, M.; Behm, R.J.; Passerini, S.; Shen, Z. Manganese phosphate coated $\text{Li}[\text{Ni}_{0.6}\text{Co}_{0.2}\text{Mn}_{0.2}]\text{O}_2$ cathode material: Towards superior cycling stability at elevated temperature and high voltage. *J. Power Sources* **2018**, *402*, 263–271. [[CrossRef](#)]
20. Choi, J.-W.; Lee, J.-W. Improved electrochemical properties of $\text{Li}(\text{Ni}_{0.6}\text{Mn}_{0.2}\text{Co}_{0.2})\text{O}_2$ by surface coating with $\text{Li}_{1.3}\text{Al}_{0.3}\text{Ti}_{1.7}(\text{PO}_4)_3$. *J. Power Sources* **2016**, *307*, 63–68. [[CrossRef](#)]
21. Liu, W.; Li, X.; Xiong, D.; Hao, Y.; Li, J.; Kou, H.; Yan, B.; Li, D.; Lu, S.; Koo, A.; et al. Significantly improving cycling performance of cathodes in lithium ion batteries: The effect of Al_2O_3 and LiAlO_2 coatings on $\text{LiNi}_{0.6}\text{Co}_{0.2}\text{Mn}_{0.2}\text{O}_2$. *Nano Energy* **2018**, *44*, 111–120. [[CrossRef](#)]
22. Liu, S.; Wu, H.; Huang, L.; Xiang, M.; Liu, H.; Zhang, Y. Synthesis of $\text{Li}_2\text{Si}_2\text{O}_5$ -coated $\text{LiNi}_{0.6}\text{Co}_{0.2}\text{Mn}_{0.2}\text{O}_2$ cathode materials with enhanced high-voltage electrochemical properties for lithium-ion batteries. *J. Alloys Compd.* **2016**, *674*, 447–454. [[CrossRef](#)]
23. Schipper, F.; Dixit, M.; Kovacheva, D.; Talianker, M.; Haik, O.; Grinblat, J.; Erickson, E.M.; Ghanty, C.; Major, D.T.; Markovsky, B.; et al. Stabilizing nickel-rich layered cathode materials by a high-charge cation doping strategy: Zirconium-doped $\text{LiNi}_{0.6}\text{Co}_{0.2}\text{Mn}_{0.2}\text{O}_2$. *J. Mater. Chem. A* **2016**, *4*, 16073–16084. [[CrossRef](#)]
24. Liu, Q.; Zhao, Z.; Wu, F.; Mu, D.; Wang, L.; Wu, B. The effects of molybdenum doping on $\text{LiNi}_{0.6}\text{Co}_{0.2}\text{Mn}_{0.2}\text{O}_2$ cathode material. *Solid State Ion.* **2019**, *337*, 107–114. [[CrossRef](#)]
25. Rao, T.; Gao, P.; Zhu, Z.; Wang, S.; Ben, L.; Zhu, Y. Structural, electrochemical, and Li-ion diffusion properties of Mg&Mn dual doped LiNiO_2 cathode materials for Li-ion batteries. *Solid State Ion.* **2022**, *376*, 115860.
26. Huang, Z.; Wang, Z.; Zheng, X.; Guo, H.; Li, X.; Jing, Q.; Yang, Z. Effect of Mg doping on the structural and electrochemical performance of $\text{LiNi}_{0.6}\text{Co}_{0.2}\text{Mn}_{0.2}\text{O}_2$ cathode materials. *Electrochim. Acta* **2015**, *182*, 795–802. [[CrossRef](#)]
27. Huang, Z.; Wang, Z.; Jing, Q.; Guo, H.; Li, X.; Yang, Z. Investigation on the effect of Na doping on structure and Li-ion kinetics of layered $\text{LiNi}_{0.6}\text{Co}_{0.2}\text{Mn}_{0.2}\text{O}_2$ cathode material. *Electrochim. Acta* **2016**, *192*, 120–126. [[CrossRef](#)]
28. Geng, C.; Rathore, D.; Heino, D.; Zhang, N.; Hamam, I.; Zaker, N.; Botton, G.A.; Omessi, R.; Phattharasupakun, N.; Bond, T.; et al. Mechanism of Action of the Tungsten Dopant in LiNiO_2 Positive Electrode Materials. *Adv. Energy Mater.* **2022**, *12*, 2103067. [[CrossRef](#)]
29. Ryu, H.H.; Park, G.T.; Yoon, C.S.; Sun, Y.K. Suppressing detrimental phase transitions via tungsten doping of LiNiO_2 cathode for next-generation lithium-ion batteries. *J. Mater. Chem. A* **2019**, *7*, 18580–18588. [[CrossRef](#)]
30. Park, G.T.; Ryu, H.H.; Park, N.Y.; Yoon, C.S.; Sun, Y.-K. Tungsten doping for stabilization of $\text{Li}[\text{Ni}_{0.90}\text{Co}_{0.05}\text{Mn}_{0.05}]\text{O}_2$ cathode for Li-ion battery at high voltage. *J. Power Sources* **2019**, *442*, 227242. [[CrossRef](#)]
31. Chen, Z.; Qin, Y.; Amine, K.; Sun, Y.K. Role of surface coating on cathode materials for lithium-ion batteries. *J. Mater. Chem.* **2010**, *20*, 7606–7612. [[CrossRef](#)]
32. Becker, D.; Borner, M.; Nolle, R.; Diehl, M.; Klein, S.; Rodehorst, U.; Schmich, R.; Winter, M.; Placke, T. Surface Modification of Ni-Rich $\text{LiNi}_{0.8}\text{Co}_{0.1}\text{Mn}_{0.1}\text{O}_2$ Cathode Material by Tungsten Oxide Coating for Improved Electrochemical Performance in Lithium-Ion Batteries. *ACS Appl. Mater. Interfaces* **2019**, *11*, 18404–18414. [[CrossRef](#)] [[PubMed](#)]
33. Xie, J.; Zhao, J.; Liu, Y.; Wang, H.; Liu, C.; Wu, T.; Hsu, P.-C.; Lin, D.; Jin, Y.; Cui, Y. Engineering the surface of LiCoO_2 electrodes using atomic layer deposition for stable high-voltage lithium ion batteries. *Nano Res.* **2017**, *10*, 3754–3764. [[CrossRef](#)]
34. Tian, F.; Zhang, Y.Z.; Liu, Z.Z.; Monteiro, R.D.; Ribas, R.M.; Gao, P.; Zhu, Y.M.; Yu, H.L.; Ben, L.B.; Huang, X.J. Investigation of structure and cycling performance of Nb⁵⁺ doped high-nickel ternary cathode materials. *Solid State Ion.* **2021**, *359*, 9. [[CrossRef](#)]
35. Jiang, J.; Eberman, K.W.; Krause, L.J.; Dahn, J.R. Structure, Electrochemical Properties, and Thermal Stability Studies of $\text{Li}[\text{Ni}_{\text{sub}0.2}\text{Co}_{\text{sub}0.6}\text{Mn}_{\text{sub}0.2}]\text{O}_{\text{sub}2}$. *J. Electrochem. Soc.* **2005**, *152*, A1874. [[CrossRef](#)]
36. Pouillier, C.; Suard, E.; Delmas, C. Structural characterization of $\text{Li}_{1-z}\text{Ni}_z\text{O}_2$ by neutron diffraction. *J. Solid State Chem.* **2001**, *158*, 187–197. [[CrossRef](#)]
37. Dahn, J.R.; Vonsacken, U.; Juzkow, M.W.; Aljanaby, H. Rechargeable LiNiO_2 /carbon cells. *J. Electrochem. Soc.* **1991**, *138*, 2207–2211. [[CrossRef](#)]
38. Bianchini, M.; Roca-Ayats, M.; Hartmann, P.; Brezesinski, T.; Janek, J. There and Back Again—The Journey of LiNiO_2 as a Cathode Active Material. *Angew. Chem.-Int. Ed.* **2019**, *58*, 10434–10458. [[CrossRef](#)]
39. Luo, D.; Fang, S.; Tamiya, Y.; Yang, L.; Hirano, S.-I. Countering the Segregation of Transition-Metal Ions in $\text{LiMn}_{1/3}\text{Co}_{1/3}\text{Ni}_{1/3}\text{O}_2$ Cathode for Ultralong Life and High-Energy Li-Ion Batteries. *Small* **2016**, *12*, 4421–4430. [[CrossRef](#)] [[PubMed](#)]
40. Hou, P.; Zhang, H.; Zi, Z.; Zhang, L.; Xu, X. Core-shell and concentration-gradient cathodes prepared via co-precipitation reaction for advanced lithium-ion batteries. *J. Mater. Chem. A* **2017**, *5*, 4254–4279. [[CrossRef](#)]
41. Ji, H.X.; Ben, L.B.; Yu, H.L.; Qiao, R.H.; Zhao, W.W.; Huang, X.J. Electrolyzed $\text{Ni}(\text{OH})_2$ Precursor Sintered with $\text{LiOH}/\text{LiNiO}_2$ Mixed Salt for Structurally and Electrochemically Stable Cobalt-Free LiNiO_2 Cathode Materials. *ACS Appl. Mater. Interfaces* **2021**, *13*, 50965–50974. [[CrossRef](#)] [[PubMed](#)]
42. Lin, Q.Y.; Guan, W.H.; Zhou, J.B.; Meng, J.; Huang, W.; Chen, T.; Gao, Q.; Wei, X.; Zeng, Y.W.; Li, J.X.; et al. Ni-Li anti-site defect induced intragranular cracking in Ni-rich layer-structured cathode. *Nano Energy* **2020**, *76*, 105021. [[CrossRef](#)]

43. Tian, F.; Ben, L.; Yu, H.; Ji, H.; Zhao, W.; Liu, Z.; Monteiro, R.; Ribas, R.M.; Zhu, Y.; Huang, X. Understanding High-Temperature Cycling-Induced Crack Evolution and Associated Atomic-Scale Structure in a Ni-rich $\text{LiNi}_{0.8}\text{Co}_{0.1}\text{Mn}_{0.1}\text{O}_2$ Layered Cathode Material. *Nano Energy* **2022**, *98*, 107222. [[CrossRef](#)]
44. Zhang, H.; Omenya, F.; Yan, P.; Luo, L.; Whittingham, M.S.; Wang, C.; Zhou, G. Rock-Salt Growth-Induced (003) Cracking in a Layered Positive Electrode for Li-Ion Batteries. *ACS Energy Lett.* **2017**, *2*, 2607–2615. [[CrossRef](#)]
45. Li, X.; Gao, A.; Tang, Z.; Meng, F.; Shang, T.; Guo, S.; Ding, J.; Luo, Y.; Xiao, D.; Wang, X.; et al. Robust Surface Reconstruction Induced by Subsurface Ni/Li Antisites in Ni-Rich Cathodes. *Adv. Funct. Mater.* **2021**, *31*, 2010291. [[CrossRef](#)]
46. Mu, L.; Lin, R.; Xu, R.; Han, L.; Xia, S.; Sokaras, D.; Steiner, J.D.; Weng, T.-C.; Nordlund, D.; Doeff, M.M.; et al. Oxygen Release Induced Chemomechanical Breakdown of Layered Cathode Materials. *Nano Lett.* **2018**, *18*, 3241–3249. [[CrossRef](#)] [[PubMed](#)]
47. Edstrom, K.; Gustafsson, T.; Thomas, J.O. The cathode-electrolyte interface in the Li-ion battery. *Electrochim. Acta* **2004**, *50*, 397–403. [[CrossRef](#)]
48. Park, O.K.; Cho, Y.; Lee, S.; Yoo, H.C.; Song, H.K.; Cho, J. Who will drive electric vehicles, olivine or spinel? *Energy Environ. Sci.* **2011**, *4*, 1621–1633. [[CrossRef](#)]
49. Fan, X.M.; Hu, G.R.; Zhang, B.; Ou, X.; Zhang, J.F.; Zhao, W.G.; Jia, H.P.; Zou, L.F.; Li, P.; Yang, Y. Crack-free single-crystalline Ni-rich layered NCM cathode enable superior cycling performance of lithium-ion batteries. *Nano Energy* **2020**, *70*, 104450. [[CrossRef](#)]
50. Yan, P.; Zheng, J.; Gu, M.; Xiao, J.; Zhang, J.-G.; Wang, C.-M. Intragranular cracking as a critical barrier for high-voltage usage of layer-structured cathode for lithium-ion batteries. *Nat. Commun.* **2017**, *8*, 14101. [[CrossRef](#)] [[PubMed](#)]
51. Ko, D.S.; Park, J.H.; Park, S.; Ham, Y.N.; Ahn, S.J.; Park, J.H.; Han, H.N.; Lee, E.; Jeon, W.S.; Jung, C. Microstructural visualization of compositional changes induced by transition metal dissolution in Ni-rich layered cathode materials by high-resolution particle analysis. *Nano Energy* **2019**, *56*, 434–442. [[CrossRef](#)]
52. Sari, H.M.K.; Li, X. Controllable Cathode-Electrolyte Interface of $\text{Li}[\text{Ni}_{0.8}\text{Co}_{0.1}\text{Mn}_{0.1}]\text{O}_2$ for Lithium Ion Batteries: A Review. *Adv. Energy Mater.* **2019**, *9*, 1901597. [[CrossRef](#)]
53. Yan, P.; Zheng, J.; Liu, J.; Wang, B.; Cheng, X.; Zhang, Y.; Sun, X.; Wang, C.; Zhang, J.-G. Tailoring grain boundary structures and chemistry of Ni-rich layered cathodes for enhanced cycle stability of lithium-ion batteries. *Nat. Energy* **2018**, *3*, 600–605. [[CrossRef](#)]
54. Min, K.; Cho, E. Intrinsic origin of intra-granular cracking in Ni-rich layered oxide cathode materials. *Phys. Chem. Chem. Phys.* **2018**, *20*, 9045–9052. [[CrossRef](#)] [[PubMed](#)]
55. Park, K.J.; Jung, H.G.; Kuo, L.Y.; Kaghazchi, P.; Yoon, C.S.; Sun, Y.K. Improved Cycling Stability of $\text{Li}[\text{Ni}_{0.90}\text{Co}_{0.05}\text{Mn}_{0.05}]\text{O}_2$ through Microstructure Modification by Boron Doping for Li-Ion Batteries. *Adv. Energy Mater.* **2018**, *8*, 1801202. [[CrossRef](#)]
56. Yin, S.Y.; Deng, W.T.; Chen, J.; Gao, X.; Zou, G.Q.; Hou, H.S.; Ji, X.B. Fundamental and solutions of microcrack in Ni-rich layered oxide cathode materials of lithium-ion batteries. *Nano Energy* **2021**, *83*, 105854. [[CrossRef](#)]